

# Recovery of fluctuation spectrum evolution from tomographic shear spectra

**Silvio A. Bonometto<sup>1,2,3</sup> & Marino Mezzetti<sup>1,2</sup>,**

<sup>1</sup> – *Department of Physics, Astronomy Unit, Trieste University, Via Tiepolo 11, I 34143 Trieste, Italy*

<sup>2</sup> – *I.N.A.F. – Astronomical Observatory of Trieste, Via Tiepolo 11, I 34143 Trieste, Italy*

<sup>3</sup> – *I.N.F.N. – Sezione di Trieste, Via Valerio, 2 I 34127 Trieste, Italy*

**ABSTRACT:** Forthcoming large angle surveys are planned to obtain high precision tomographic shear data. In principle, they will allow us to recover the spectra of matter density fluctuation, at various redshift, through the inversion of the expressions yielding shear from fluctuation spectra. This was discussed in previous work, where *SVD* techniques for matrix inversion were also shown to be the optimal tool to this aim. Here we show the significant improvements obtainable by using a 7 bin tomography, as allowed by future *EUCLID* data, as well as the question of error propagation from shear to fluctuation spectra. We find that the technique is a promising tool, namely for the analysis of baryon physics through high- $\ell$  shear spectra and to test the consistency between expansion rate and fluctuation growth.

**KEYWORDS:** cosmology: theory, dark matter, gravitation; methods: numerical, N-body & hydrodynamic simulations..

---

## Contents

<b>1. Introduction</b>	<b>1</b>
<b>2. Evaluation of shear–shear correlation functions</b>	<b>3</b>
<b>3. Density fluctuation and shear spectra</b>	<b>6</b>
<b>4. From fluctuation to shear spectra</b>	<b>7</b>
4.1 Spectra interpolation	7
4.2 The simulation	9
4.3 Gauss–Laguerre integration procedure	10
<b>5. Formal inversion</b>	<b>10</b>
<b>6. The SVD technique</b>	<b>12</b>
6.1 Singularity level	12
6.2 Recovery in the absence of noise	14
6.3 Recovery in the presence of noise	17
<b>7. Discussion</b>	<b>18</b>
<b>8. Conclusions</b>	<b>21</b>

---

## 1. Introduction

Dark Energy (DE) is one of the main discoveries – and puzzles – in contemporary physics. Cosmic Microwave Background spectra or Baryonic Acoustic Oscillations directly constrain its contribution to the cosmic budget, but only simultaneous low- $z$  measures of cosmic expansion rate and fluctuation growth can provide us real clues on DE nature [1]. In fact, besides of its state equation  $w(z)$ , we aim at knowing whether DE is a further physical dark component, or its observations are a signal of new physics, as GR violations [2], interactions between the dark components, possibly suggesting a unified picture for them [3, 4], or even more exotic scenarios [5, 6]. It is then worth outlining that, while SNIa data constrain the expansion rate, tomographic shear data can enable us to follow the growth of density inhomogeneities, matching it with background geometry, namely if such data can be suitably shared in a number of redshift bins. Moreover, being directly sensitive to the whole mass distribution, shear data allow us to forget any problem related to light–mass conversion.

In order to exploit this kind of data, it has become customary to follow a Bayesian approach. We then consider a set of parameters spanning a wide model set, for each of whom a number of observables can be predicted; prediction are then compared with observational data and relative errorbars, so obtaining likelihood hyper-ellipsoids in the parameter space. Similarly, when cosmic shear data will be available, one shall predict the tomographic shear spectra  $C_{ij}(\ell)$  for the models considered (an operational definition of  $C_{ij}(\ell)$  is given below; let us soon outline, however, that the indices  $i, j$  run on the tomographic bins) and enrich the fit to data by comparing them with tomographic shear data.

In a previous paper ([7], Paper I herebelow) we considered a somehow different option: directly deriving the fluctuation spectra  $P(k, z)$  at various redshift  $z$  from the tomographic shear spectra  $C_{ij}(\ell)$ . If doing so, a prediction of shear spectra is no longer required, and shear data can be soon compared with other data on density fluctuation growth, to be then used in parallel with them. This option makes sense, in particular, if we wish to inspect background geometry and fluctuation dynamics separately.

In the literature, an integral relation yielding  $C_{ij}(\ell)$  from  $P(k, z)$  has been known since long. A procedure to invert it has been introduced in Paper I. There, however, we restricted our analysis to 5 tomographic bins, while EUCLID<sup>1</sup> data, obtained from a celestial area of 15,000 square degrees with a median redshift  $z_m = 0.9$ , will allow N-bin tomography, with  $N \gg 5$  and up to 10 [8].

In this paper, we consider a 7 bin tomography and find that the improvements allowed by this  $N$  increase, when aiming to recover  $P(k, z)$ , are substantial. The recovery still uses the singular value decomposition (SVD) technique for matrix inversion. Specific options of this technique, suitable to treat quasi-singular matrices, will be however used here for the first time in this context. Furthermore, we shall treat the question of noise propagation from shear to fluctuation spectra. Matrix theory allows us to predict upper limits to error magnification in such transition. Luckily enough, in this specific case, such limits are only marginally approached, while a simple filter allows us further noise reduction.

Let us also notice that, besides of verifying the coherence between expansion and fluctuation growths, this inversion technique could also facilitate the discrimination between different options on baryon physics, shaping  $P(k, z)$  at high- $k$ .

In order to test the inversion algorithm we need to input fluctuation spectra for a given model. We use them to build fluctuation spectra  $P(k, z)$  at various redshifts and then, from these spectra, the tomographic shear spectra  $C_{ij}(\ell)$ . Successively, starting from  $C_{ij}(\ell)$ , we test how efficiently  $P(k, z)$  is recovered, under various options. Being also interested in baryon physics and, therefore, having to explore the high- $\ell$  region, hydrodynamical simulations are to be used. A brief discussion on the simulations used will be therefore provided. Let us however preliminarily outline that the lensing spectra can be roughly shared in 3  $\ell$ -ranges (see Figure 3, here below): The  $C_{ij}(\ell)$  for  $\ell < \sim 500$  essentially feel just the linear dynamics, even for  $i, j = 1$ . For  $500 < \ell < 1500$  the contribution coming from *non-linear*  $k$ 's becomes relevant. At  $\ell > 2000$ , shear data start to exhibit a dependence on

---

<sup>1</sup>[www.euclid-ec.org](http://www.euclid-ec.org)

baryon physics.

The plan of the paper is as follows: In the next Section we shall review the procedure allowing to pass from data on galaxy ellipticity to shear spectra. In particular, we shall obtain the window function in the 7-bin case, taking into account that, for most lensed galaxies, only the photometric redshift can be given.

In Section 3 the fluctuation and shear spectra will be defined and their relation set in an operational form. Section 4 consists of three discussions: on the simulation used; on the pattern followed to interpolate its outputs, so obtaining  $P(k, z)$  at the prescribed  $k$  and  $z$  values; on the procedure of Gauss–Laguerre integration to pass from fluctuation to shear spectra. Section 5 introduces the formal procedure to invert the equation yielding  $C_{ij}(\ell)$  from  $P(k, z)$ , also based on the Gauss–Laguerre procedure. Section 6 then introduces the SVD technique and uses it for the study of the singularity level, as well to recover  $P(k, z)$  from  $C_{ij}(\ell)$ , in 3 cases: (i) When  $C_{ij}(\ell)$  is formally obtained with a GL integration technique. (ii) When  $C_{ij}(\ell)$  is “exact”. (iii) When noise is added to it. Results are summarized and discussed in Section 7 and conclusions are drawn in Section 8, where we also outline possible options to improve the present approach.

## 2. Evaluation of shear–shear correlation functions

The procedure to derive shear spectra starts from approximating galaxy images by ellipses of axes  $a$  and  $b$  ( $a > b$ ), and setting

$$\gamma = \gamma_+ + i\gamma_\times \equiv \frac{a^2 - b^2}{a^2 + b^2} e^{2i\psi}, \quad (2.1)$$

in agreement with [9], [10]. Here  $\psi$  is the angle between the major axis of the ellipse and the  $x$ -axis of a chosen coordinate system on the sky, assumed to be locally flat. When the galaxy sample occupy a wide celestial area, as in the case of EUCLID, it can be necessary to correct for the sky curvature [11].

Measuring galaxy ellipticity is a non-trivial task, but the main problem is that ellipticities are not due to gravitational shear only. The so-called *intrinsic* shear due to nearby galaxy alignment is the main problem while, aiming at correlating galaxy ellipticities, the presence of an uncorrelated random shear component is not so critical. Assuming that data can be simply and reliably cleansed from intrinsic alignment may be premature (see however [12], [13] and references therein), but here we let apart this problem and proceed as though  $\gamma$  were due to gravitational shear only.

Measures will be considered in the context of (spatially flat) models whose background metric reads

$$ds^2 = a^2(\tau)[d\tau^2 - d\lambda^2], \quad (2.2)$$

so that  $\tau$  is the conformal time,  $d\lambda$  being the comoving distance element, and  $a(\tau) \equiv (1+z)^{-1}$  the scale factor. If  $\tau_0$  is the present conformal time,

$$u(z) = \tau_0 - \tau(z) \quad (2.3)$$

is the conformal time distance from the redshift  $z$ . Owing to eq. (2.2) it is also the comoving distance from  $z$ .

According to data, we then assume that galaxies observed in unit solid angle, on the light cone of this space-time, have a normalized distribution on redshift reading

$$n(z) = \frac{d^2 N}{d\Omega dz} = \mathcal{C} \left( \frac{z}{z_0} \right)^A \exp \left[ - \left( \frac{z}{z_0} \right)^B \right] \quad (2.4)$$

with

$$\mathcal{C} = \frac{B}{[z_0 \Gamma(\frac{A+1}{B})]} \quad (2.5)$$

and  $A = 2$ ,  $B = 1.5$ , so that  $\mathcal{C} = 1.5/z_0$  (with  $z_0 = z_m/1.412$  obtained from the median redshift  $z_m = 0.9$ , in agreement with EUCLID specifications [8]). These phenomenological values can however be suitably modified, if needed.

In order to appreciate the effects of fluctuation evolution, observed galaxies are then shared into  $N$  redshift bins, with limits  $z_r$  possibly selected so that each of them contains an equal number of galaxies. However, if we want the galaxy set to be large, we must accept that only their photometric redshifts are available.

To evaluate the expected distribution on redshift for the  $r$ -th bin galaxies, we must then apply the filter

$$\begin{aligned} \Pi_r(z) &= \int_{z_r}^{z_{r+1}} dz' \frac{1}{\sqrt{2\pi} \sigma(z)} \exp \left[ - \frac{(z - z')^2}{2\sigma^2(z)} \right] = \\ &= \frac{1}{2} \left[ \text{Erf} \left( \frac{z_{r+1} - z}{\sqrt{2}\sigma(z)} \right) - \text{Erf} \left[ \frac{z_r - z}{\sqrt{2}\sigma(z)} \right] \right] \end{aligned} \quad (2.6)$$

to  $n(z)$  (through this paper we shall take  $\sigma(z) = 0.05(1+z)$ , coherently with EUCLID expectations [8], see also [14]), so obtaining the distribution

$$D_r(z) = n(z) \Pi_r(z) . \quad (2.7)$$

whose integral is  $\simeq 1/N$ , while their sum is (exactly)  $n(z)$ , as shown in Figure 1.

The images of the galaxies belonging to a bin are lensed by the gravity of matter laying at lower  $z$ . This is taken into account by defining the *window functions*

$$W_r(z) = \frac{3}{2} \Omega_m (1+z) \int_{\Delta z_r} dz' \delta_r(z') \mathcal{P} \left[ \frac{u(z') - u(z)}{u(z')} \right]; \quad (2.8)$$

here  $u(z) = \tau_0 - \tau(z)$  and

$$\delta_r(z) = \frac{D_r(z)}{\int_0^\infty D_r(z') dz'} \quad (2.9)$$

is obtained by normalizing each  $D_r$  to unity, and the integration can be restricted to the interval  $\Delta z_r$ , where  $D_r$  is significantly  $> 0$ ; let also be  $\mathcal{P}(x) = x$  or  $0$  if  $x > 0$  or  $< 0$ : only systems closer than a galaxy can distort its image. Window functions for the 7-bin case are shown in Figure 2.

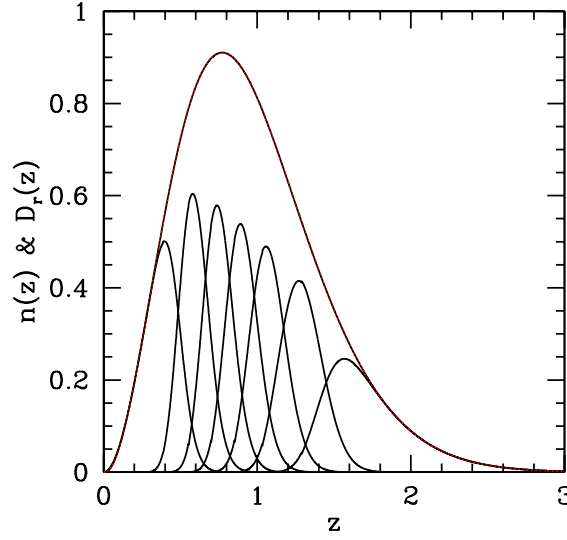


**Figure 1:** Total galaxy distribution  $n(z)$  (red curve) and distributions  $D_r(z)$  of the galaxies in  $N = 7$  bins as obtainable through photometric redshift values. Their sum (black dots) overlaps  $n(z)$ .

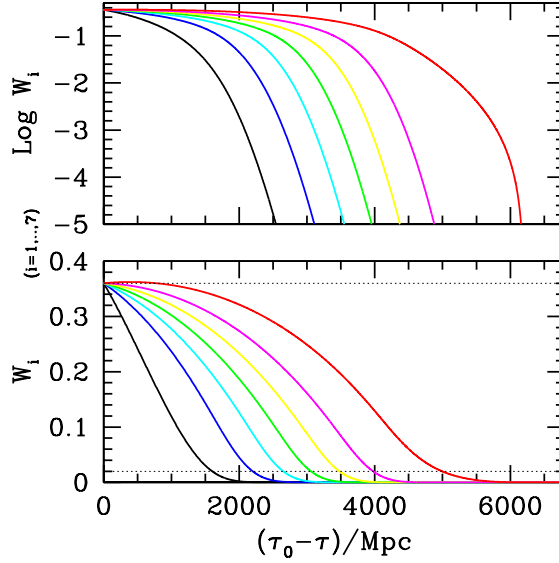


**Figure 2:** Window functions for the 7-bin case. In the spatially flat models considered, along the light cone, conformal time delay and comoving distance coincide.

In order to calculate the window functions  $W_r$  through the expression (2.8) we need to know the  $u(z)$  dependence, i.e., the background geometry. More in general, the reference cosmology in this paper is a  $\Lambda$ CDM model with density parameters for total matter and baryons, Hubble parameter, primordial spectral index and the mean square amplitude of linear density fluctuations, at  $z = 0$ , on the scale of  $8 h^{-1} \text{Mpc}$ , shown herebelow in Table I:

Table I

$\Omega_m$	$\Omega_b$	$h$	$n_s$	$\sigma_8$
0.24	$4.13 \times 10^{-2}$	0.73	0.96	0.8

However, as far as building  $W_r$  is concerned: (i) no knowledge of baryon physics is needed, not even the  $\Omega_b$  value; (ii) no parameters ruling the dynamics, as  $\sigma_8$  or  $n_s$ , are to be known. The cosmology described by Table I is the same of Paper I.

The shear–shear correlation functions among galaxy pairs can then be estimated through the sums

$$\xi_{+/-}^{ij}(\theta) = \frac{\sum_{\alpha\beta} [\gamma_{+;\alpha}^i \gamma_{+;\beta}^j + / - \gamma_{\times;\alpha}^i \gamma_{\times;\beta}^j] \Theta_{\alpha\beta}}{\sum_{\alpha\beta} \Theta_{\alpha\beta}} \quad (2.10)$$

( $\alpha$  and  $\beta$  run over the galaxy set), by sharing the angle  $\theta$  into bins, and setting  $\Theta_{\alpha\beta} = 1/0$  when the angle  $\theta_{\alpha\beta}$  between galaxy images is within/outside the suitable bin.

### 3. Density fluctuation and shear spectra

The shear–shear correlation functions can be expanded in spherical harmonics on the celestial sphere. It can then be shown that

$$\xi_{+/-}^{ij}(\theta) = (2\pi)^{-1} \int_0^\infty d\ell \ell J_{0/4}(\ell\theta) C_{ij}(\ell), \quad (3.1)$$

with the same angular spectrum  $C_{ij}(\ell)$  ( $J_n$  being first kind Bessel functions of order  $n$ ). Owing to the finiteness of the celestial sphere, the modulus of a 2–dimensional wave vector  $\ell$  would be allowed just discrete values. However, the contribution from the  $\ell$ –th component is roughly due to shear on the angular aperture  $\vartheta \sim 2\pi/\ell$ , and we do not expect shear signals to be significant at large– $\vartheta$ .

Here, as usual, the Fourier transform of the density fluctuation field  $\epsilon(\mathbf{x}, z) = [\rho(\mathbf{x}, z) - \bar{\rho}(z)]/\bar{\rho}(z)$  reads

$$\delta(k, z) = \frac{1}{(2\pi)^3} \int d^3x e^{i\mathbf{k}\cdot\mathbf{x}} \epsilon(\mathbf{x}, z) \quad (3.2)$$

and, at any redshift  $z$ , we define the power spectrum  $P(k, z) = \langle |\delta(k, z)|^2 \rangle$ . Then, it can be shown that the relation

$$C_{ij}(\ell) = H_0^4 \int_0^{\tau_0} du W_i(u) W_j(u) P[\ell/u, u] \quad (3.3)$$

holds. Here and in what follows, both  $P(k, z)$  and  $P(k, u)$  will be used, the latter symbol indicating  $P[\ell/u, z(u)]$ , as in eq. (3.3). The  $W_i(u)$  are the window functions defined in eq. (2.8). Here again notice the rough correspondence  $k \sim 2\pi/\lambda$ .

It is reasonable to expect that the contributions to the shear on an angular scale  $\vartheta$  depend on density fluctuations over the increasingly large scale  $\lambda$  subtended by  $\vartheta$ , as  $z$  increases. Accordingly, eq. (3.3) shows that the shear signal at a given  $\ell$  receives contributions from decreasing  $k$  values as  $u$  increases. In principle, for  $u \rightarrow 0$ ,  $P(k, u)$  should be

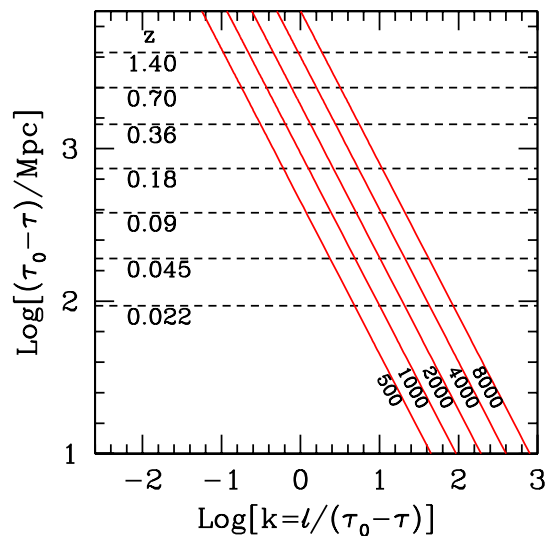


**Figure 3:** The red lines show the  $k$  values contributing to the  $C_{ij}(\ell)$  shear spectra at constant  $\ell$  (aside them) and growing redshift.

evaluated at  $k \rightarrow \infty$  where, however, it vanishes.

If we consider the  $\log k$ - $\log u$  plane, the integration in eq. (3.3) is carried along tilted straight lines as those shown in Figure 3, each line corresponding to a given  $\ell$ .

The spectra  $P(k, z)$  therefore yield functions  $P_\ell(u) = P[\ell/u, z(u)]$  with  $\ell$  fixing a straight line on the  $\log k$ - $\log u$  plane and  $u$  being an abscissa on such line.

## 4. From fluctuation to shear spectra

Our aim now amounts at finding a technique allowing the inversion of eq. (3.3). To do so, we shall first work out the spectra  $C_{ij}(\ell)$  for a given model, according to eq. (3.3) itself. In the linear range there is no problem to obtain the function  $P_\ell(u) = P[\ell/u, z(u)]$ , for any  $u$  and  $\ell$ , from algorithms like CAMB. On the non-linear range one has then to make recourse to simulations, which however yield  $P(k = \ell/u, u)$ , on a set of points  $k_b$ - $u_a$  (redshift values  $z_a$ ).

### 4.1 Spectra interpolation

There is then an interpolation problem, to work out  $P_\ell(u)$  in the points needed for integration. While integration routines are very efficient and allow any required precision, the actual precision depends on how interpolation is performed among the limited set of points available.

To do it, there are at least 3 different patterns, schematically shown in Figure 4. We can first work out  $P_\ell(u_a)$  at fixed  $\ell$ , by interpolating among  $k_b$  values. To perform the integral we need  $P_\ell(u)$  for suitable values of  $u \neq u_a$ , and this is obtainable by further interpolating at constant  $\ell$ . In Figure 4 the pattern 1 outlines this procedure. (It may be worth outlining that, here and in the next cases, interpolation does not only involve the 2



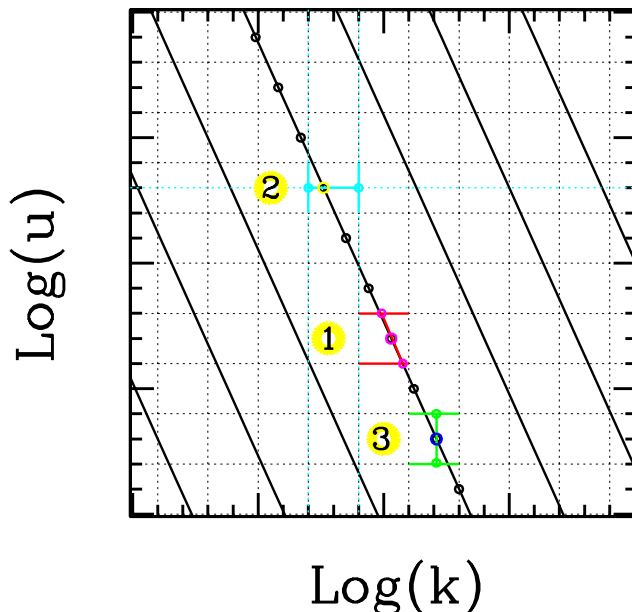


**Figure 4:** Interpolation patterns. This schematic Figure assumes that “data” are available at the crossings between horizontal and vertical dotted lines. The tilted lines are at constant  $\ell$ . Along one of them, we schematically indicate a set of points where we need to know  $P(l, u)$ , to perform the numerical integration. To reach them, in any case, there are 2 interpolation steps. The direction of former (latter) is indicated by the two parallel segments (a single segment, tilted or orthogonal).

closest points in each direction. The thick segments in the Figure are to be taken just as an indication of directions along which one uses a cubic spline.)

Otherwise, we can first determine  $P(k_b, u)$  at the  $u$  value needed and then we interpolate at constant  $u$  along  $k$  (pattern 2).

The third option considered is determining first  $P(k, u_a)$  at the  $k$  value needed; then we interpolate at constant  $k$  along  $u$  (pattern 3).

In order to test which procedure is best, we made use of the HALOFIT algorithm, yielding spectra at arbitrary  $k$  and  $u$ . This allowed us to appreciate that the procedures 2 & 3 are substantially equivalent. On the contrary, the procedure 1, requiring interpolation along the tilted  $\ell$ -constant curves, yields consistent results only when spectra are known at many more redshift values  $z_a$  (approximately 3 times more).

A similar procedure was also used to test that the  $k$  and  $z$  number where we have simulation “data” is adequate; as a matter of fact, it turns out to be so only if we avoid the first interpolation pattern.

The integration interval in eq. (3.3) is apparently finite. When  $u$  reaches the conformal age of the Universe  $\tau_0$ , however,  $z$  approaches  $\infty$ . Figure 2 shows that all  $W_i$  vanish well before so, and this sets an effective upper limit to the integration.

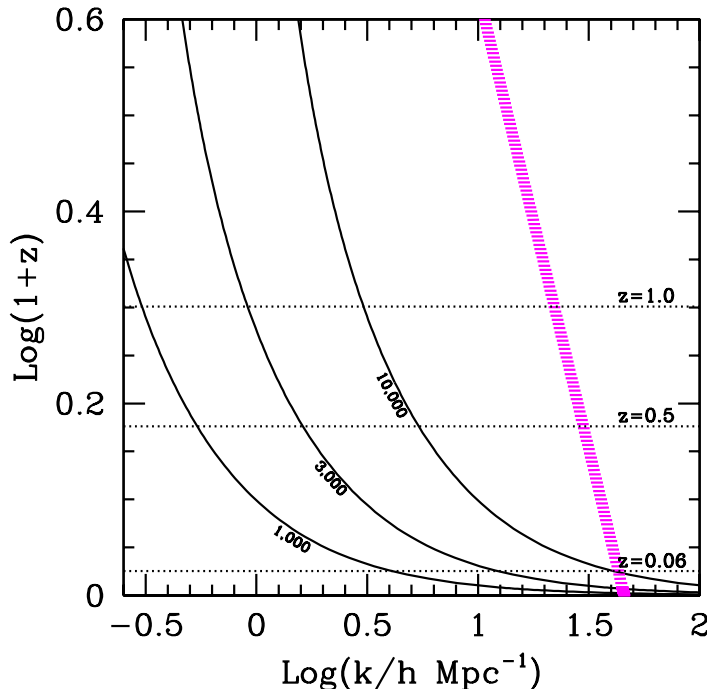


**Figure 5:** The magenta dashed line sets the  $k$  upper limit above which shot noise covers physical spectra. The black curves are the integration patterns for the  $\ell$  values indicated aside them (at variance from the previous Figure, due to the different ordinate, here they are not straight lines). The horizontal dashed lines indicate are at  $z = 0.06, 0.5, 1$ . Accordingly, even the power spectra needed to obtain shear spectra at  $\ell = 10000$  are free of shot noise as soon as  $z > \sim 0.06$ , corresponding to  $\sim 17.5 h^{-1}\text{Mpc}$ .

Aiming at 5-digit precision, a numerical integration performed by summing on a large number of equispaced points requires  $\sim 2000$  points up to  $u \sim 6000$  ( $z \sim 3$ ), paying attention that each contributions added to the sum is sufficiently large in respect to numerical precision.

## 4.2 The simulation

Let us give now some information on the simulation used. More details are given in [15]. The simulation was run in a box of side  $L = 410 h^{-1} \text{Mpc}$  (corresponding to  $k_L \sim 1.5 \times 10^{-2} h\text{Mpc}^{-1}$ ) where  $(2 \times) 1024^3$  particles were set, and with a force resolution  $\epsilon = 7.5 h^{-1} \text{kpc}$  (corresponding to  $k_\epsilon \sim 8.4 \times 10^2 h\text{Mpc}^{-1}$ ). More precisely, spectra can be used up to  $k \simeq N(2\pi/L)$  with  $N \simeq 2^{15} = 32768$ , however keeping  $k (\simeq 5.0 \times 10^2 h\text{Mpc}^{-1}) < k_\epsilon$ , provided that they are not covered by shot noise (see Figure 5).

Being hydrodynamical, two populations of particles are used in simulations. With the cosmological parameter of Table I, the masses of CDM and baryonic particles are  $m_c \simeq 1.89 \times 10^9 h^{-1} M_\odot$  and  $m_b \simeq 3.93 \times 10^8 h^{-1} M_\odot$ , respectively. The baryon dynamics includes the effect of cooling and star formation. A description of metal production from chemical enrichment contributed by SN-II, SN-Ia and AGB stars, as described in [16], is also included. Stars of different mass, distributed according to a Salpeter IMF, release metals

over the time-scale determined by the corresponding mass-dependent life-times. Kinetic feedback is also implemented by mimicking galactic ejecta powered by SN explosions. In these simulations AGN feedback is not included, at variance from [17], where smaller simulation boxes are however kept. Simulation start at  $z = 41$  and spectra are obtained for the redshift values

$$1 + z_r = 10^{r/20} \quad (r = 1, \dots, 19) . \quad (4.1)$$

8 of them, up to  $z \simeq 1.24$  are between 0 and 1.4; 7 more are within  $z = 4.02$ . These 15 spectra are used for interpolation.

### 4.3 Gauss–Laguerre integration procedure

Besides of performing “exact” Riemann integration, here we need to consider a Gaussian integration procedure as well. It amounts to projecting each integrand function  $f(u) = W_i(u)W_j(u) P_\ell(u)$  onto polynomials  $\pi_\alpha(u)$ , orthogonal with an assigned weight function  $R(u)$ , finding its components  $f_\alpha$ . As the integrals  $\Pi_\alpha$  of each polynomial are known, the integral of  $f(u)$  reads  $\sum_{\alpha=1}^N f_\alpha \Pi_\alpha$ , and this is a reliable value if  $N$  is large enough. For practical aims, this technique can be translated into a simple procedure, i.e. to a weighted sum of values taken by the integrand function  $f(u)$  in a suitable set of points  $u_\alpha$ .

More in detail, using *monic* polynomials, we have that

$$\int_0^\infty dx R(x) \pi_\alpha(x) \pi_\beta(x) = \mathcal{N} \delta_{\alpha\beta} , \quad (4.2)$$

with a known normalization  $\mathcal{N}$ . Monic polynomials are obtained from a suitable recurrence relation assuming that the coefficient of the leading term, for each  $\alpha$ , is unity. If we then truncate the sum to  $N$  terms, the  $N$  zero’s of  $\pi_N(x)$  are the points  $x_\alpha$ , while the corresponding weights are

$$w_\alpha = \frac{\int_0^\infty dx R(x) \pi_{N-1}^2(x)}{\pi_{N-1}(x_\alpha) \pi'_N(x_\alpha)} , \quad (4.3)$$

$\pi'(x)$  being the ordinary derivative of  $\pi(x)$ . It is then

$$\int_0^\infty du f(u) = \int_0^\infty dx F(x) R(x) = \sum_\alpha w_\alpha F(x_\alpha) \quad (4.4)$$

with

$$F(x) = f[u(x)](du/dx)/R(x) . \quad (4.5)$$

For  $R(x) \propto e^{-x}$ , this technique is dubbed Gauss–Laguerre integration, as  $\pi_\alpha(x) = L_\alpha(x)$ , the Laguerre polynomials. In the case of eq. (3.3), where integration is cut off by the decay of the  $W_i$  functions, this approach can be applied by assuming  $x = (u/\bar{u})^\beta$  and suitably selecting then  $\bar{u}$  and  $\beta$ .

## 5. Formal inversion

Let us then rewrite eq. (3.3) as follows:

$$c_A(\ell) = \sum_{r=1}^N w_r S_{Ax_r} p_{x_r}(\ell) \equiv \sum_{r=1}^N \mathcal{M}_{Ar} p_r(\ell) . \quad (5.1)$$

Here we have set

$$A \equiv ij, \quad c_A = C_{ij}/H_0^4 \quad (5.2)$$

with the correspondence law

$i, j$	1, 1	...	1, 7	2, 2	...	2, 7	3, 3	...	...	7, 7
$A$	1	...	7	8	...	13	14	...	...	28

while, by setting  $u_r = u(x_r)$ , we have

$$S_{Ax_r} = W_i(x_r)W_j(x_r)u_r/[\beta x_r R(x_r)], \quad (5.3)$$

$$p_r(\ell) \equiv p_{x_r}(\ell) = P_\ell(u_r) = P(\ell/u_r, u_r). \quad (5.4)$$

If, in eq. (5.1), we take  $N = 28$ ,  $\mathcal{M}_{Ar}$  are square matrices and, provided that they are not singular, the inverse equation

$$p_{x_r}(\ell) = \sum_A (\mathcal{M})_{rA}^{-1} c_A(\ell) \quad (5.5)$$

also holds. In principle, we should then be able to work out the spectrum  $P(k, z)$  for any  $k = \ell/u_r$ , at the redshift values  $z_r = z(u_r)$ .

Notice that the inversion procedure acts on each  $\ell$  value separately. Any  $z$  and/or  $k$  value can be attained, in principle, just by suitably choosing the  $\bar{u}$  and  $\beta$  parameter. In principle, we could perform a different choice for each  $\ell$ .

This procedure was first introduced in Paper I, where  $N$  could reach atmost 15. This led to 2 difficulties: (i) 15 gaussian points were far from allow a nearly-exact integration; (ii) the determinant of the  $15 \times 15$   $\mathcal{M}$  matrix was close to singular.

Curiously enough, an inversion could be attained by passing from 15 to 12 integration point. Although worsening the (i) point, this allowed to formulate a redundant system of equations, which could then be treated by using the SVD technique. A suitable choice of  $\bar{x}$  and  $\beta$  allowed then to overcome the (ii) points and to achieve an exact inversion of the  $C_{ij}(\ell)$  spectra formally obtained through Gaussian integration.

As a matter of fact, however, even this was not yet enough when trying to invert the results of exact integration (i.e., the Riemann integration): some  $P(k, z)$  were recovered, in fact, but systematically ill-normalized. As a matter of fact, however, once the cosmological parameters needed to build the  $W_r(u)$  are known, one needs to add just  $\Omega_b$  and  $\sigma_8$  to predict the exact normalization (the dependence on  $n_s$  was found to be negligible). In this way one could work out all the details of the high- $k$  spectra  $P(k, z)$  from  $C_{ij}(\ell)$ , once the linear part of  $P(k, z)$  is known. However, the need to add information on baryonic and dynamical parameters is not much welcome.

Here we aim to test whether we can do better if up to 28 indipendent equations are allowed, *a priori*. In particular, no input concerning baryonic and/or dynamical parameters will be sought, any more.

## 6. The SVD technique

The risk of singularity for the matrix

$$\mathcal{M}_{Ar} = w_r W_{i(A)}(x_r) W_{j(A)}(x_r) u_r / [\beta x_r R(x_r)] \quad (6.1)$$

arises from the vanishing of  $W_i$  –for low  $i$  values– when  $u_r - x_r$  attain values where  $W_i$  –for high  $i$  values– is still significant. Let us then introduce the SVD technique which, first of all, allows us to evaluate the degree of singularity of a matrix.

The SVD technique is based on a theorem of linear algebra, stating that any real  $N_r \otimes N_c$  matrix  $\mathcal{M}$ , with  $N_r \geq N_c$ , can be decomposed, in a unique way apart trivial overall factor shifts, into a rows  $\times$  columns product

$$\mathcal{M}_{N_r, N_c} = \mathcal{U}_{N_r, N_c} \times | \text{diag}(s_i) |_{N_c} \times \mathcal{V}_{N_c, N_c}^T \quad (6.2)$$

Here, in each index site, we set the range allowed to the index there. Both  $\mathcal{M}$  and  $\mathcal{V}$  ( $\mathcal{V}^T$  is its transposed) are orthonormal matrices; also  $| \text{diag}(s_i) |_{N_c}$  is a (fully diagonal) matrix.

If  $N_r = N_c$ , the inverse of  $\mathcal{M}$ , in general, reads

$$\mathcal{M}^{-1} = \mathcal{V} \times | \text{diag}(1/s_i) | \times \mathcal{U}^T, \quad (6.3)$$

and, as we shall discuss shortly, the technique is also a valid numerical way, not only to invert large matrices, but also to handle them when their full inversion is numerically impossible. A fair discussion of the SVD technique can be found in *Numerical Recipes* [18] or in *Matrix Computations* [19].

The degree of singularity, however, can be inspected by considering the  $s_i$  components. When some of them vanishes, the matrix is singular and the problem is said to be *ill-conditioned*. Even if it is not so, as in our cases, it may happen that the ratio between the greatest and smallest  $s_i$  (condition number) exceeds  $\sim 10^6$  ( $10^{12}$ ), and then there is no hope to invert  $\mathcal{M}$  in *single* (*double*) precision. Anyhow, if a level of precision  $\mathcal{O}(1 : 10^5 - 10^6)$  is to be achieved, *double* precision is surely needed, so to keep the top  $s_i/s_j$  ratio within  $\sim 10^6 - 10^7$ . This being necessary condition, it turns out not to be a sufficient one and, quite often, we need to be more restrictive.

### 6.1 Singularity level

With 28 equations available our first attempt was to invert a  $28^2$  matrix. As expected, its degree of singularity depends on the choice of  $\bar{u}$  and  $\beta$ . Best results are obtainable, as we discuss in Appendix A, when the top  $z_r$  value is  $\sim 1.40$  and the low- $z$  domain is sampled above  $z \sim 0.05$ .

In this paper, we shall consider the case  $\bar{u} = 351$ ,  $\beta = 1.8424$ . In Figures 6 and 7 we plot the Gaussian weights vs. the related redshift values and the components of the diagonal matrix  $s$  obtained. Let us remind that each  $w_r$  is multiplied by  $e^{x_r}$ , so that also  $w_r \sim 10^{-40}$  are not negligible. On the contrary, the  $s_i$  components do span more than 13 o.o.m. and inverting the  $\mathcal{M}$  matrix, as it is, would therefore require unusual computational resources.

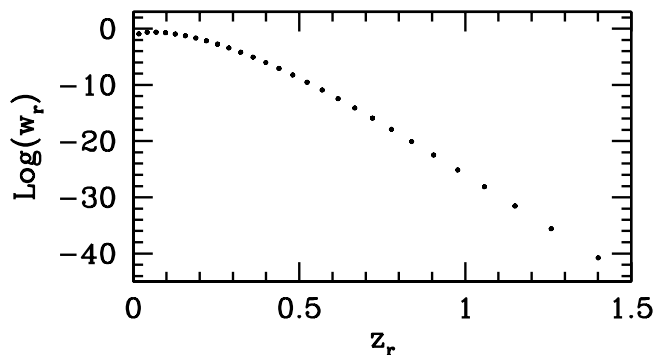


**Figure 6:** Gauss–Laguerre weights vs. the related redshift values.

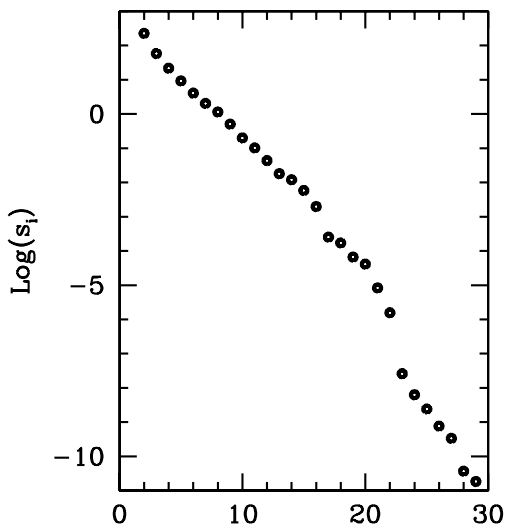


**Figure 7:** The elements  $s_i$  of the diagonal matrix, yielding the singularity level of the matrix to be inverted.

The SVD approach however tells us how to deal with this case keeping as much information as possible from the matrix while reducing its effective singularity level. We can do so simply by setting to zero the unwanted  $s_i$  values. For instance, if we set to zero the last 7 (8)  $s_i$ , the residual component are within 9 (8) orders of magnitude. The rationale of this reduction of the condition number is explained in the cited manuals and discussed in Appendix A; it does not coincide with simply disregarding a number of equations, as the power spectra are actually recovered at all 28 redshifts, although discrepancies from input fluctuation spectra are safely small for  $0.1 \sim z \sim 1.2$ . As a matter of fact, this is the very range where shear signals are reliable, and the matrix inversion technique substantially yields a best-fit recovery of input spectra.

There is however another point deserving to be soon outlined. Real data on  $C_{ij}(\ell)$  spectra will come with error bars. For practical application this is the critical point. In order to study their effect, we shall therefore add a random Gaussian noise to the  $C_{ij}(\ell)$

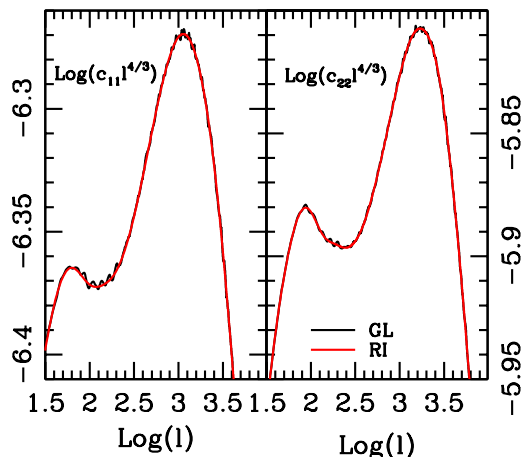


**Figure 8:** GL and RI integration compared.

spectra obtained by integrating the fluctuation spectra. In the inversion process, noise tends to be magnified: in Appendix B we show that an upper limit to noise magnification is approximately set by the ratio between the top and bottom  $s_i$  which were not set to zero. Therefore, using  $s_i$  spanning 8 orders of magnitude is likely to yield  $C_{ij}(\ell)$  spectra completely covered by noise.

This is a reason why we shall need to exploit the SVD technique at its limits, by keeping just a few non-zero  $s_i$ . Luckily enough the transferred noise, in this case, is significantly below the theoretical upper limit and can be furtherly reduced by filtering.

In the next subsections we shall provide quantitative details on these points.

## 6.2 Recovery in the absence of noise

Two different integration techniques have been considered here: (i) a Riemannian technique (RI, hereafter) allowing any wanted precision; (ii) a Gauss–Laguerre technique (GL, hereafter), that opens the door to the inversion.

Although using 28 points and coefficients, GL does not fully succeed to recover the  $C_{ij}(\ell)$  spectra obtained by RI. As a matter of fact, the spectra from simulations are not completely smooth and keep small fluctuations even for small  $k$  increments. Even a 28-th degree polynomial is unable to follow all of them.

In Figure 8 we compare the results of GL and RI integration for  $C_{11}(\ell)$  and  $C_{22}(\ell)$  (the coefficient  $H^4$  is omitted). These plots are aimed to magnify the differences, which are  $\mathcal{O}.1\%$  at most, but can be clearly perceived. Notice, in particular, that the GL integrals exhibit tiny oscillations. When GL integration is performed by using a more usual number of points ( $\sim 10$ ), these oscillations risk to be confused with the effect of BAO's in fluctuation spectra. A similar danger exists if we perform a RI integration after an interpolation of type 1 with not enough spectra along  $z$ . In this case BAO's are an effect of the interpolating polynomials and disappear when we increase the number of spectra along  $z$ .

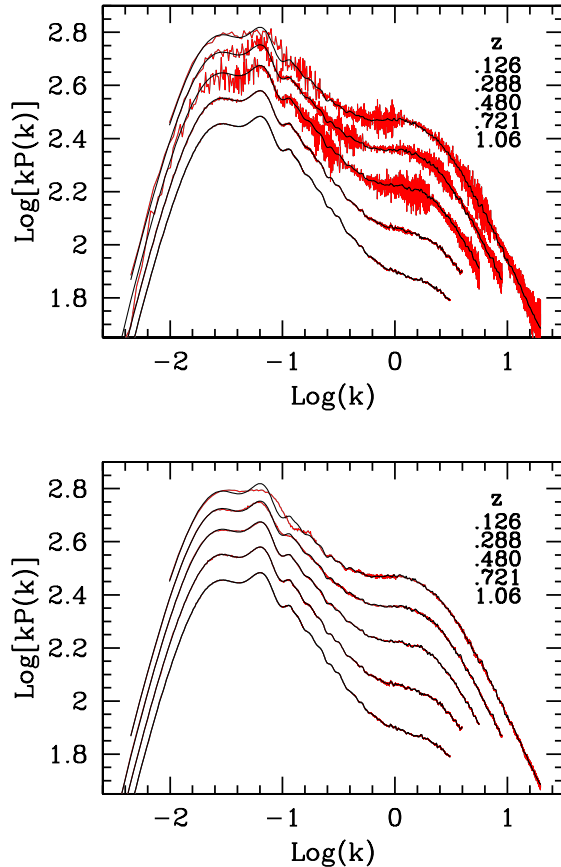


**Figure 9:** Recovery of  $P(k, z)$  spectra, at the 5 redshifts shown in the frames (chosen for the sake of example), by using GL shear spectra and 21 (upper frame) or 20 (lower frame) non-zero  $s_i$ . Black curves are the input spectra. The red curves are the spectra recovered; in some cases, namely for 20- $s_i$ , the recovery is so efficient that the red lines are almost canceled by the black input spectra.

In Figure 9 we show the results of matrix inversion if applied to GL spectra, using 20 or 21  $s_i$  values. The passage from 9 to 8 o.o.m. in the  $s_i$  selection appears to be critical. Notice also that the algorithm has however some difficulty to recover the BAO shape, namely at low  $z$ . In the 21- $s_i$  case, we see the low- $z$  spectra covered by the numerical noise.

In Figure 9 and in the following ones we plot a selection of spectra, for the  $z_i$  values shown in the frame. For the sake of homogeneity, redshifts are the same in all Figures. Notice that, rather than selecting those redshifts where the inversion algorithm performs best, we provide equi-spaced values starting from a range where inversion just begins to work. Among the values plotted, there are  $\sim 20$  (mostly unplots) redshift values where spectra are recovered in a fashion similar to the best results shown.

Let us now test the results of applying the inversion algorithm, based on GL integration,



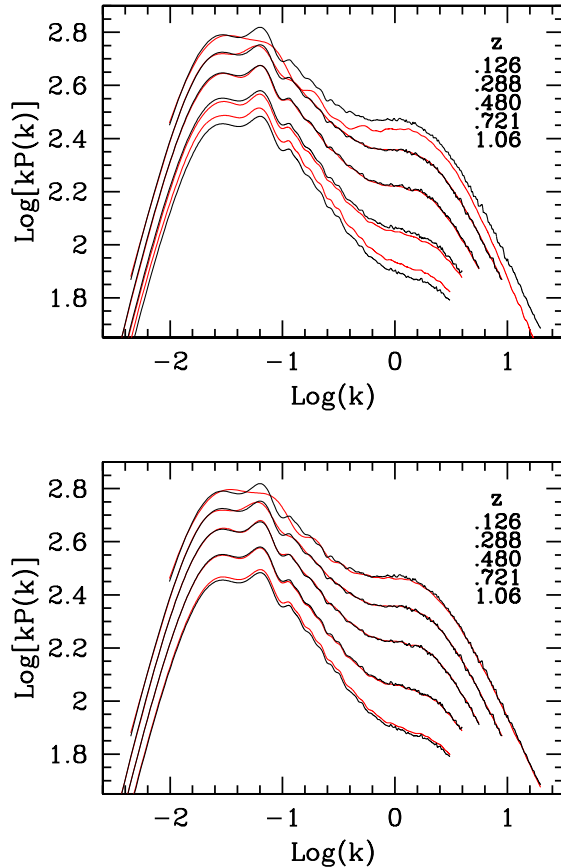


**Figure 10:** Recovery of  $P(k, z)$  spectra, at the 5 redshifts shown in the frames (the same as in the previous Figure), by using RI shear spectra and 16 (upper frame) or 15 (lower frame) non-zero  $s_i$ . Black and red curves as in the previous Figure.

on RI spectra. In this case, the transition from unsuitable to fair spectra occurs at the passage from 16 to 15  $s_i$  values. Unsatisfactory inversion is however appreciable here through curve confusion, rather than by curves obscured by numerical noise. The inversion is slightly less precise, typical errors being  $\mathcal{O}(1\%)$ , apart of the BAO range, where recovery still appears more critical; the degree of precision will be debated in detail when in the presence of noise.

Before concluding the discussion on inversion in the absence of noise, let us consider also the case of keeping just 6  $s_i$ , shown in Figure 11.

This Figure witnesses the high efficiency of the SVD technique, allowing to recover a large deal of spectra by apparently using just 6 equations. As a matter of fact, in the redshift range 0.2–1, fluctuation spectra are recovered with errors keeping  $\mathcal{O}(1\%)$  in most of the  $k$  range; unfortunately, however, BAO's tend to be badly recovered and the low- $k$

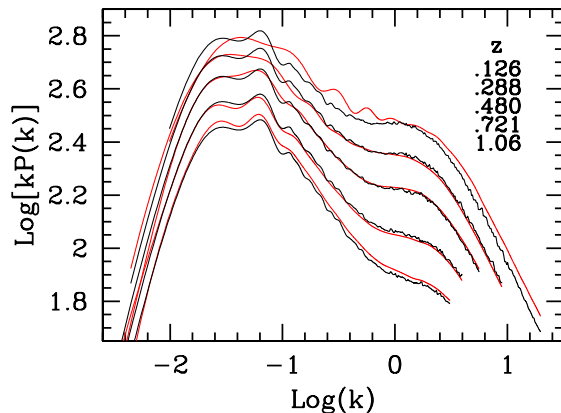


**Figure 11:** Recovery of  $P(k, z)$  spectra, at the same 5 redshifts of previous Figures, starting from RI shear spectra and keeping just 6 non-zero  $s_i$ . Black and red curves as in the previous Figures.

range is significantly problematic.

### 6.3 Recovery in the presence of noise

The study of error propagation from  $C_{ij}(\ell)$  to  $P(k, z)$  spectra is one of the main contribution of this work. As above mentioned, in the process of matrix inversion errors expand. We shall however show that, suitably modeling available parameters, this expansion can be kept under control. The case considered here should be however considered just as a good example. Further improvement is likely to be still possible, by refining the  $\bar{u}$ - $\beta$  selection or passing to a more sophisticated mapping from  $u$  and  $x$  variables. Also the noise initially found in recovered  $P(k, z)$  spectra will be filtered here in a simple fashion. More efficient filtering will be certainly possible.

Moreover, while the 7-bin case is already significant, the huge improvement found by passing from 5 to 7 bins suggests a further increase in the bin number, at the limits allowed by shot noise.

Bearing all that in mind, let us consider Figure 12. Here we started from  $C_{ij}(\ell)$  spectra obtained from an “exact” Riemann integration. From it we derived the “noisy” spectrum

$$C_{ij}^{(N)}(\ell) = C_{ij}(\ell) \times [1 + \varepsilon G] . \quad (6.4)$$

Here  $G$  is a random variable distributed in a Gaussian way around zero, with unit variance;  $\varepsilon$  then sets the effective m.s.d.; in Figure 12 results obtained for  $\varepsilon = 0.8\%$  will be shown (cyan curves). Results are then filtered by using a 10-point top-hat filter (red curves). The basic SVD inversion is achieved here by keeping just 6 non-zero  $s_i$ . This allows us to keep  $\mathcal{O}(\sim 300)$  the ratio between top and bottom non-zero  $s_i$  (condition number) and this is the theoretical upper limit to error magnification. In face of these predictions, we find that, in the central  $z$ -range and after filtering, errors can be reduced to  $\sim 5\%$ , therefore keeping the typical error magnification well within a factor  $\sim 10$ . This unexpected success is one of the results of this analysis.

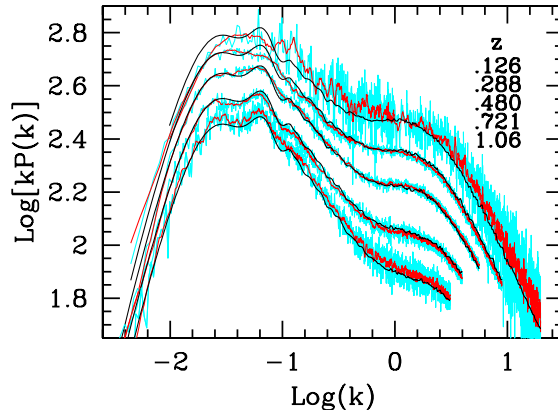


**Figure 12:** Recovery of  $P(k, z)$  spectra, at the same 5 redshifts of previous Figures, starting from RI shear spectra and keeping just 6 non-zero  $s_i$ . The black curves, as in previous Figures, show the input fluctuation spectra. The results of inverting noisy shear spectra are the cyan curves. By applying to them a simple-minded top-hat filter, averaging among 10 nearby  $k$  values, errors are smoothed and we obtain the red curves.

In the rest of this Section we show the errors by plotting the ratios between recovered and input  $P(k, z)$  for 12 equispaced values of  $z$ . We shall consider the SVD inversions obtained by using 7, 6, and 5 non-zero  $s_i$ . The Figures 13 these ratios are shown. In each Figure, 3 redshift values (shown aside) are considered by using 3 different colors. Each plot can be associated to the related redshift by reminding that, when  $z$  increases, the  $k$ -range, for which  $P(k, z)$  is recovered, shifts to smaller values. The recovered spectra were again smoothed by averaging over 10 nearby points. This rough filter already yields a significant error reduction. More sophisticated filters could certainly allow to gain an extra factor 2, at least.

As expected, reducing the number of non-zero  $s_i$  reduces error magnification. In order to achieve a tolerable error magnification, however, the number of non-zero  $s_i$  needs to be small. According to Figure 13, taking 6 non-zero  $s_i$  (over 28) appear to be the best compromise: further reducing the non-zero  $s_i$  number starts to affect significantly  $P(k, z)$  normalization; keeping more non-zero  $s_i$  further magnifies errors.

This is also confirmed by Figure 14, which shows the average shifts and the variance about them for the points 2–27. This Figure shows a sort of oscillatory residuals, reminiscent of the use of a finite number of orthogonal polynomials. Let us also notice that, if an improved filtering further reduces errorbars, using 7 non-zero  $s_i$  could also be a fair choice, as oscillatory residuals decrease when the number of non-zero  $s_i$  is greater.

With such low numbers of non-zero  $s_i$ , recovering the BAO shape appears however difficult; in the low  $k$ -range the inversion seems to work poorly.

## 7. Discussion

In this paper we discuss the inversion of the integral expression yielding the tomographic

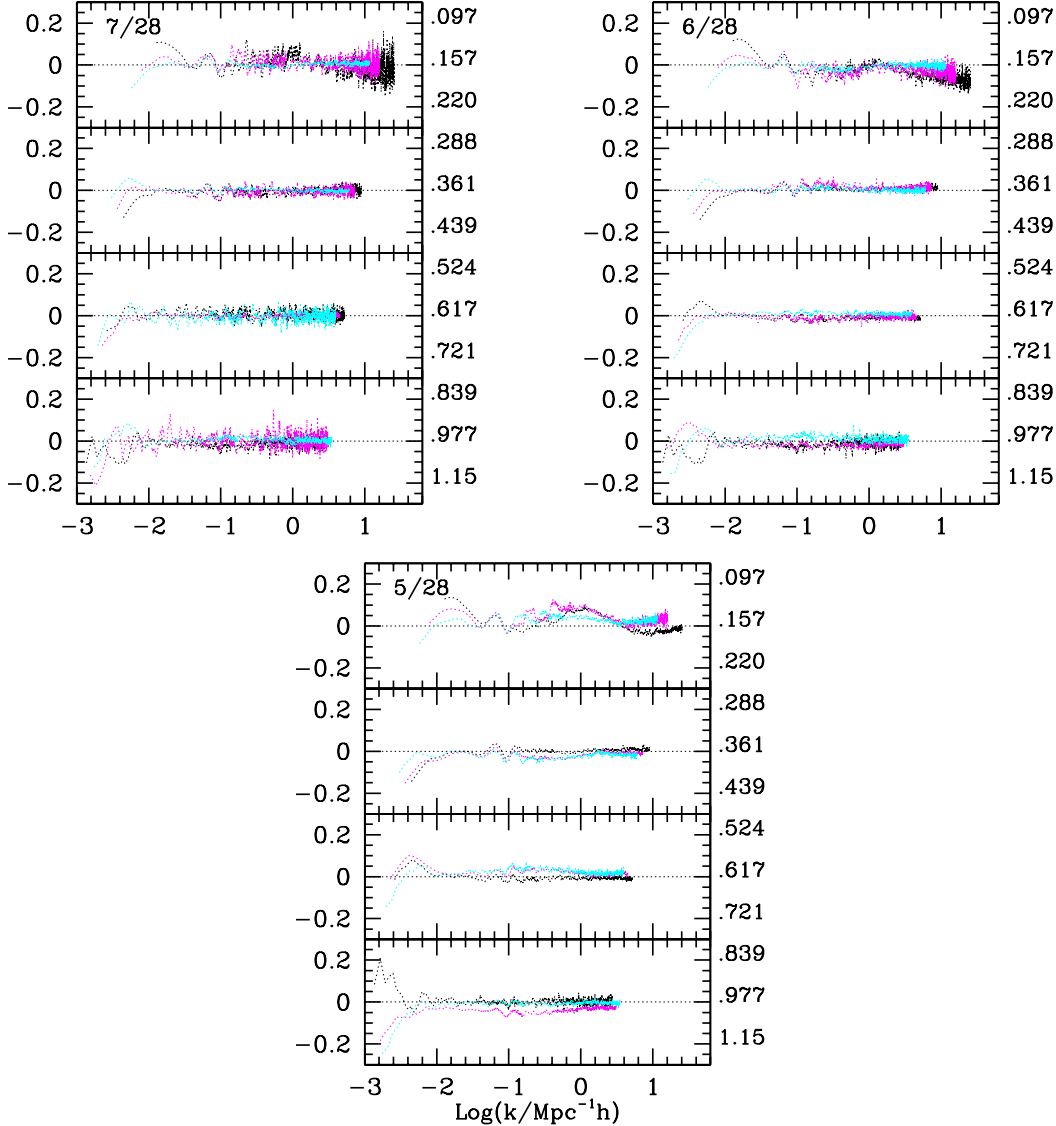


**Figure 13:** Ratio between recovered and input power spectra at different redshifts (at the r.h.s. of the Figures), when the shear spectra is added a Gaussian noise  $\sim .8\%$ . The recovered spectra were filtered through a 10-point top-hat smoothing. The Figures are obtained when 7, 6, 5 non-zero  $s_i$  are kept. Reducing the number of non-zero  $s_i$  reduces error magnification, but biases the inversion process. In the case considered, best results seem obtainable with 6 non-zero  $s_i$ . See also the next Figure.

shear spectra  $C_{ij}(\ell)$  from the density fluctuation spectra  $P(k, z)$ . In a previous work (Paper I), the question had been discussed with  $(N=)5$  bin tomography, yielding  $N(N+1)/2=15$  independent shear spectra. With present samples, spreading shear data over 5 bins yields spectra already seriously affected by shot noise. We however expect future data (EUCLID) to cover a larger sky portion, so allowing up to 10 bin tomography.

We however kept below this limit and considered here  $N=7$ , yielding  $N(N+1)/2=28$  independent shear spectra. This already allows us great improvements in respect to  $N=5$ . Another contribution of this work is the study of noise propagation from tomographic shear

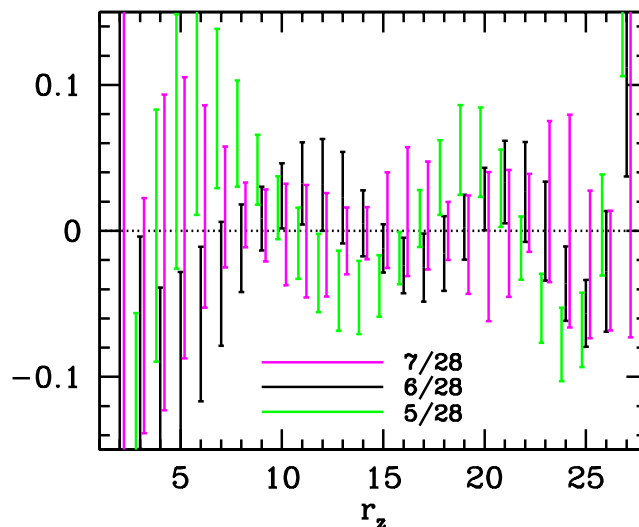


**Figure 14:** Average displacements from unity of the ratios between input and recovered spectra; m.s. oscillation amplitudes around average are shown by errorbars.

data to fluctuation spectra.

We have started from the equation yielding shear from fluctuation spectra in the form

$$c_A = \mathcal{M}_{A,r} p_r . \quad (7.1)$$

Here  $C_{ij}(\ell) \equiv H^4 c_A(\ell)$  and  $p_r(\ell) = P(u_r/\ell, u_r)$ ,  $u$  being the comoving distance of the redshift  $z$ . Let us remind that fluctuation spectra used here were obtained by suitably connecting linear and hydro simulation spectra, according to a technique widely discussed in Paper I. The basic issue here is that we need no approximate spectral expression (like HALOFIT) to perform a fairly normalized connection, thanks to the wide box ( $410 h^{-1} \text{Mpc}$ ) used in simulations. Eq. (7.1) deals with each  $\ell$  separately; summation replaces there integration and is performed by using a Gauss–Laguerre (GL) technique, involving the replacement of the comoving distance variable  $u$  with

$$x = (u/\bar{u})^\beta , \quad (7.2)$$

and approximating the large- $u$  behavior of integrand functions by  $\exp(-x)$ . As  $A$  takes 28 values, we are allowed a 28-point GL integration; the sum (7.1) then closely approaches the exact integral. Tiny residual differences however remain, which will matter in the discussion below. The matrix  $\mathcal{M}$  is obtained from the expected galaxy distribution on  $z$ , the bin structure, the photometric–spectrographic redshift relation, and the space geometry.

Recovering  $P(u_r/\ell, u_r)$  from  $C_{ij}(\ell)$  then requires inverting the matrix  $\mathcal{M}$ . Unfortunately, as different bins refer to different depths,  $\mathcal{M}$  approaches a singular behavior.

The recovery of  $P(k, z)$  is therefore based on the singular value decomposition (SVD) technique for matrix inversion. Such technique soon yields the degree of singularity through the elements of a  $28 \times 28$  diagonal matrix  $s$ . Singularity however depends on the choice of

the parameters  $\bar{u}$  and  $\beta$  and, in this work, we provide an analysis of the criteria for their selection. No full  $\mathcal{M}$  matrix can be however inverted with standard numerical means, as the  $s_i$  diagonal components of the matrix  $s$  span  $\sim 13$ – $14$  o.o.m., in spite of optimizing the  $\bar{u}$ – $\beta$  selection. (A look at the Figure in Appendix A however shows that an unsuitable parameter choice can yield  $s_i$  spanning many more o.o.m.’s.)

According to the SVD technique, we can however reduce the divergence level, by setting to zero a number of  $s_i$ . This is similar – but not fully equivalent and, indeed, not so drastic – to suppressing a number of equations. Our analysis greatly exploits this option, also in view of the fact that also error propagation depends on the ratio between minimum and maximum non-zero  $s_i$ .

The simplest task that the inversion procedure can accomplish is the recovery of  $P(k, z)$  from  $C_{ij}(\ell)$  obtainable via GL integration. The only limitation that we meet, in this case, is the divergence degree outlined by the diagonal  $s$  matrix components. Out of 28  $s_i$  components, we find that best results are obtainable when keeping 20 non-zero  $s_i$ . Already with 21 components, numerical noise affects the low- $z$  recovered spectral components.

We then tested the inversion of the results of exact integration. Although being closer to realistic, this works as though adding a noise to the  $c_A(\ell)$  components. As a matter of fact, to obtain fair results, we must then furtherly reduce the number of non-zero  $s_i$ . Best results are obtained with 15  $s_i$  components. Typical discrepancies between input and output fluctuation spectra are then  $\mathcal{O}(1\%)$ , apart of some wider discrepancy arising in the low- $k$  BAO range, namely for low redshift.

These results are however a great improvement in respect to 5 bins. Then, the very normalization of recovered spectra was at risk and fair results could be obtained only through renormalization in the low- $k$  range.

We then tested error propagation by superimposing a Gaussian noise (m.s.a.  $\sim 0.8\%$ ) onto the  $C_{ij}(\ell)$  spectra obtained from the integration of simulation spectra. Such noise is however magnified by matrix inversion. A theoretical upper limit on noise magnification is set by the ratio between the top and bottom  $s_i$  kept (see Appendix A). This calls for pushing further down the number of non-zero  $s_i$ . As a matter of fact, best results are obtained when keeping 6 non-zero  $s_i$  (over 28!). If 7 are kept, the error is greater. If we try to keep just 5 of them, we meet displacements on recovered spectrum normalization.

The noise in direct inversion results was then tentatively filtered by using a 10-point top-hat smoothing. After using this admittedly rough smoothing technique, we find that the overall noise magnification is less than a factor 10, in respect of a theoretical upper limit  $\sim 300$ . Let us also outline that spectral values on nearby  $k$  values derive from independent  $\ell$  inputs, so that filtering acts in a “normal” direction, in respect to matrix inversion.

The  $k$ -region most penalized by the suppression of a large number of  $s_i$  is the BAO range. Here errors are greater and we can summarize our outputs by saying that this technique does not allow to recover the BAO structure.

## 8. Conclusions

Shear data are expected to be a new and effective resource to discriminate among cosmo-

logical models. They are most sensitive to the rate of expansion and fluctuation growth at low- $z$ , when the contribution of Dark Energy is determinant. Accordingly, they are expected to be an outstanding probe on the DE equation of state  $w(z)$  and/or to possible deviation from GR, or to couplings between the dark cosmic components.

From data we expect tomographic shear spectra to be derived. A basic difficulty amounts to cleansing rough data from intrinsic ellipticities. This fundamental question is relevant for our present aims just because it might constrain the number  $N$  of tomographic bins used. In fact, to our aims, using  $N = 7$  is found to yield much better results than  $N = 5$  or less.

An analysis of spectral data can be performed in accordance with a Bayesian paradigm. In this context,  $C_{ij}(\ell)$  model predictions will be made, and compared with  $C_{ij}(\ell)$  data and their errorbars.

Other sets of data, possibly derived from the same EUCLID experiment, will directly concern the  $P(k, z)$  spectra.

The possibility to skip  $C_{ij}(\ell)$  model predictions, by directly using the  $P(k, z)$  spectra obtained from them, together with other data on  $P(k, z)$ , could then be appealing, although it is hard to state, at this stage, if error magnification is an obstacle to this option.

In order to build the  $\mathcal{M}$  matrix, that shall be inverted to work out  $P(k, z)$  from  $C_{ij}(\ell)$ , we must be able to convert redshifts into comoving distances. This requires some information on the model *geometry*, but no dynamical or baryonic information: neither  $\sigma_8$  and  $n_s$ , nor parameters describing baryon physics (including  $\Omega_b$ ) or cosmic reionization shall be input.

For the sake of example, let us then outline a possible investigation pattern: SNIa data could become so good that the distance modulus could provide  $u(z)$  with negligible errors. From such  $u(z)$  the parameters of the background cosmology can be derived. However, independently from such derivation, we could directly use  $u(z)$  to build the window functions  $W_r$  and derive from them the inverted matrix  $\mathcal{M}^{-1}$ , so obtaining  $P(k, z)$  – apart of a constant factor  $(\Omega_m H_0^2)^2$  – and the fluctuation growth law  $G(a)$ . In parallel with fitting  $u(z)$  to models, we then also fit  $G(a)$  to them, so performing two independent model tests, based on geometry and dynamics, respectively. Altogether, the two tests could provide a direct confirm/falsification of models where DE and DM are two real and independent cosmic components.

More in general, this technique allows us to measure the fluctuation growth in an unbiased way, over any  $k$ -range, namely those where different hypotheses on stellar formation, SN explosion, AGN energy release, etc., are critical. Accordingly, the inversion technique might become an important tool to discriminate among different hypotheses on baryon physics, possibly testing parameters beyond those spanning the bayesian parameter space.

Let us finally outline that there is a substantial space for further improvements of the technique providing  $P(k, z)$  from shear spectra. We wish to outline, in particular, the following points: (i) We saw the great improvement achieved when passing from  $N=5$  to  $N=7$ ; here we did not test greater  $N$  values, but it is licit to expect that further improvements are at hand if using 8, 9, or 10 bins is possible. Although EUCLID is expected to provide a tomography with up to 10 bins, it is not clear to us up to which point intrinsic shear

cleansing is more effective with  $N = 5$  or less. (ii) Noise propagation was considered here to test error propagation. Propagated errors were then filtered, with a procedure effective but rough. Better filtering techniques are surely available, but selecting among them depends on the actual nature of the “noise” to be considered. (iii) A specific technical issue concerns the passage from the comoving distance  $u$  to the integration coordinate  $x$ . Changes in the parameters  $\bar{u}$  and  $\beta$  entering in the conversion expression  $x = (u/\bar{u})^\beta$  were found to be critical, and an optimal parameter choice to be almost determinant. Let us then outline that  $u$ - $x$  mappings more effective than a simple power law, namely in the low- $x$  range, could also allow us further substantial improvements.

**ACKNOWLEDGMENTS.** SAB acknowledges the support of CIFS. We are grateful to Stefano Borgani for making available to us his large hydrodynamical simulations and to Volker Springel for the non-public GADGET-3 code used to run them. Giuseppe La Vacca is also gratefully thanked for a number of useful discussions. H. Hoekstra, T. Kitching, L. Guzzo and W. Percival are also to be thanked for comments.

## References

- [1] Albrecht A. et al. 2006, Report of the Dark Energy Task Force, APS meeting abstract, APR, G1002; also: arXiv:astro-ph/0609591
- [2] S. Capozziello, S. Nojiri, S. D. Odintsov and A. Troisi, Phys. Lett. B 639 (2006) 135; L. Amendola, D. Polarski, and S. Tsujikawa, *Are  $f(R)$  dark energy models cosmologically viable?* Phys. Rev. Lett. 98 (2007), 131302; L. Amendola, R. Gannouji, D. Polarski and S. Tsujikawa, Phys. Rev. D 75 (2007) 083504; P. Creminelli, G. D’Amico, J. Norena, & F. Vernizzi, *The Effective Theory of Quintessence: the  $w < -1$  Side Unveiled*, J. of Cosm. & Astrop. Phys. 0902 (2009) 018; M. Park, K. M. Zurek, and S. Watson, *A Unified Approach to Cosmic Acceleration*, Phys. Rev. D 81 (2010) 124008; J. K. Bloomfield and E. E. Flanagan, *A Class of Effective Field Theory Models of Cosmic Acceleration*, J. of Cosm. & Astrop. Phys. 10 (2012) 039;
- [3] T. Damour, Gibbons G. W., Gundlach C., Phys.Rev.Lett. 64 (1990) 123 ; C. Wetterich , A&A, 301 (1995) 321; Amendola L. Phys.Rev.D 62 (2000) 643511; Amendola L., Quercellini C., Phys Rev D68 (2001) 023514; N. Dalal, K. Abazajian, E. E. Jenkins, and A. V. Manohar, *Testing the cosmic coincidence problem and the nature of dark energy*, Phys. Rev. Lett. 87 (2001), 141302; Amendola L., Tocchi Valentini D. Phys. Rev. D66 (2002) 041528; Andrea V. Maccio’, Claudia Quercellini, Roberto Mainini, Luca Amendola, Silvio A. Bonometto, *N-body simulations for coupled dark energy: halo mass function and density profiles*, Phys.Rev.D69 (2004) 123516; Roberto Mainini, Silvio A. Bonometto, *Dark Matter and Dark Energy from the solution of the strong CP problem*, Phys.Rev.Lett. 93 (2004) 121301; Roberto Mainini, Silvio Bonometto, *Mass functions in coupled Dark Energy models*, Phys.Rev.D74 (2006) 043504; Mainini Roberto, Silvio Bonometto, *Dark Matter & Dark Energy from a single scalar field: CMB spectrum and matter transfer function*, JCAP 0709 (2007) 017; Roberto Mainini, Silvio Bonometto, *Limits on coupling between dark components*, JCAP 0706 (2007) 020; L.P.L. Colombo, R. Mainini, S. A. Bonometto, *Do WMAP data favor neutrino mass and a coupling between Cold Dark Matter and Dark Energy?* G. La Vacca, J.R. Kristiansen,



- JCAP 0904 (2009) 007; Roberto Mainini, *Voids and overdensities of coupled Dark Energy*, JCAP 0904 (2009) 017; J. R. Kristiansen, G. La Vacca, L. P. L. Colombo, R. Mainini, S. A. Bonometto, *Coupling between cold dark matter and dark energy from neutrino mass experiments*, New Astron.15 (2010) 609; W. Zimdahl, D. Pavon, and L. P. Chimento, *Interacting quintessence*, Phys. Lett. B 521 (2001), 133; S. del Campo, R. Herrera, G. Olivares, and D. Pavon, *Interacting models of soft coincidence*, Phys. Rev. D 74 (2006), 023501; H. Wei and S. N. Zhang, *Observational  $H(z)$  data and cosmological models*, Phys. Lett. B 644 (2007), 7; L. Amendola, G. C. Campos, and R. Rosenfeld, *Consequences of dark matter-dark energy interaction on cosmological parameters derived from SN Ia data*, Phys. Rev. D 75 (2007), 083506; Z. K. Guo, N. Ohta, and S. Tsujikawa, *Probing the coupling between dark components of the universe*, Phys. Rev. D 76 (2007), 023508; G. Caldera-Cabral, R. Maartens, and L. A. Urena-Lopez, *Dynamics of interacting dark energy*, Phys. Rev. D 79 (2009), 063518; Valeria Pettorino, Luca Amendola, Carlo Baccigalupi, Claudia Quercellini, *Constraints on coupled dark energy using CMB data from WMAP and SPT*, arXiv:1207.3293
- [4] M.C. Bento, O. Bertolami, *Dark energy and the Rutherford-Soddy radiative decay law* Phys.Lett.B675 (2009) 231; M.C. Bento, R. Gonzalez Felipe, *The variation of the electromagnetic coupling and quintessence*, Phys.Lett.B674 (2009) 146-151; M.C. Bento, R. Gonzalez Felipe, N.M.C. Santos *Brane assisted quintessential inflation with transient acceleration* , Phys.Rev. D77 (2008) 123512.
- [5] K. Tomita, *Distances and lensing in cosmological void models*, Astrophys. J. 529 (2000), 38; M. N. Celerier, *Do we really see a cosmological constant in the supernovae data?*, A & A 353 (2000) 63; K. Tomita, *A local void and the accelerating universe*, Mon. Not. Roy. Astron. Soc. 326 (2001), 287; H. Iguchi, T. Nakamura, and K. i. Nakao, *Is dark energy the only solution to the apparent acceleration of the present universe?*, Prog. Theor. Phys. 108 (2002), 809; R. Jimenez, P. Talavera, & L. Verde, *An effective theory of accelerated expansion*, arXiv:1107.2542
- [6] T. Buchert, *Dark energy from structure A status report*, Gen. Rel. Grav. 40 (2008) 467; S. Rasanen, *Dark energy from backreaction* JCAP 0402 (2004) 003; E. W. Kolb, S. Matarrese, A. Notari, and A. Riotto, *The effect of inhomogeneities on the expansion rate of the universe*, Phys. Rev. D 71 (2005) 023524; E. W. Kolb, S. Matarrese, and A. Riotto, *On cosmic acceleration without dark energy*, New J. Phys. 8 (2006) 322; C. M. Hirata and U. Seljak, *Can superhorizon cosmological perturbations explain the acceleration of the universe?*, Phys. Rev. D 72 (2005), 083501; P. Martineau and R. H. Brandenberger, *The effects of gravitational back-reaction on cosmological perturbations*, Phys. Rev. D 72 (2005) 023507; A. Ishibashi and R. M. Wald, *Can the acceleration of our universe be explained by the effects of inhomogeneities?*, Class. Quant. Grav. 23 (2006), 235; M. Kasai, H. Asada, and T. Futamase *Toward a no-go theorem for accelerating universe by non-linear backreaction*, Prog. Theor. Phys. 115 (2006) 827; S. Rasanen, *The effect of structure formation on the expansion of the universe*, Int. J. Mod. Phys. D 17 (2009) 2543; F. Piazza, *Modifying gravity in the infra-red by imposing an ultra-strong equivalence principle*, arXiv:hep-th/0904.4299 (2009); F. Piazza, *The IR-completion of gravity: What happens at Hubble scales?*, New J. Phys. 11 (2009) 113050; V. Silveira & I. Waga, *Decaying Lambda cosmologies and power spectrum*, Phys. Rev. D 50 (1994) 4890.
- [7] Mezzetti Marino, Bonometto Silvio A., Casarini Luciano & Murante Giuseppe, *Direct recovery of fluctuation spectra from tomographic shear spectra*, JCAP.06 (2012) 005 (Paper I)
- [8] Laureijs R. et al., 2012, SPIE Proceedings 8442, 32; Refregier A., Amara A., Kitching T. D., Rassat A., Scaramella R., Weller J., et al. 2010, [arXiv:1001.0061]

- [9] Kamionkowski M., Kosowhy B. & Stebbins A., Phys. Rev. D55 (1997) 7368
- [10] Crittenden R.G., Natarajan P., Pen U. & Theuns T. , *Spin-induced Galaxy Alignments and Their Implications for Weak-Lensing Measurements*, ApJ 559 (2001) 552; Huterer D., 2002, Phys. Rev. D 65, 063001; Huterer D. and Takada M., 2005, Astropart. Phys. 23, 369.
- [11] Stebbins A., *Weak Lensing On the Celestial Sphere*, astro-ph/9609149
- [12] Schrabback T. et al., *Evidence of accelerated expansion of the Universe from weak lensing tomography with COSMOS*, A&A 516 (2010) 63
- [13] Joachimi B. & Bridle S.L., *Simultaneous measurement of cosmology and intrinsic alignments using joint cosmic shear and galaxy number density correlations*, 2010, A&A 523, A1
- [14] Amara A. & Refrégier A., 2007, MNRAS 381, 1018; Amendola L., Kunz M. & Sapone D., JCAP 0804 (2008) 013
- [15] Casarini L., Bonometto S. A., Borgani S., Dolag K., Murante G., Mezzetti M., Tornatore L., La Vacca G., *Tomographic weak-lensing shear spectra from large N-body and hydrodynamical simulations*, A&A 542 (2012) 126
- [16] Tornatore L., Borgani S., Dolag K. & Matteucci F., *Chemical enrichment of galaxy clusters from hydrodynamical simulations*, MNRAS 382 (2007) 1050
- [17] Semboloni E., Hoekstra H., Schaye J., van Daalen M.P., McCarthy I.G., 2011, arXiv:1105.1075; *Quantifying the effects of baryonic physics on weak lensing tomography*, MNRAS 417 (2012) 2020; see also: Semboloni E., Hoekstra H., Schaye J., arXiv:1210.7303 *Effects of baryonic feedback on two and three point shear statistics: prospects for detection and improved modeling*.
- [18] Press W.H., Teukolsky S.A., Vetterling W.T. & Flannery B.P., 1992, *Numerical Recipes*, Cambridge Univ. Press, par. 2.6 .
- [19] Golub G.H. & Van Loan C.F., 1989, *Matrix Computations*, J.Hopkins Univ. Press, par. 5.2.6 .
- [20] G.M. Phillips & P.J. Taylor, *Theory and Applications of Numerical Analysis*, Academic Press, 2<sup>nd</sup> Edition, 1996; L.N. Trefethen & D. Bau III, *Numerical Linear Algebra*, Society for Industrial and Applied Mathematics (SIAM), Philadelphia, 1997

## Appendix A

### 1. The singular value decomposition (SVD)

The SVD technique is based on a theorem of linear algebra stating that any  $M \times N$  ( $M > N$ ) matrix  $\mathcal{M}$  can be decomposed in the matrix product  $U \cdot s \cdot V^T$  (here  $V^T$  is the transpose of a matrix  $V$ ) or, more in detail,

$$\begin{vmatrix} \mathcal{M}_{11} & \dots & \mathcal{M}_{N1} \\ \dots & \dots & \dots \\ \mathcal{M}_{1M} & \dots & \mathcal{M}_{NM} \end{vmatrix} = \begin{vmatrix} U_{11} & \dots & U_{N1} \\ \dots & \dots & \dots \\ U_{M1} & \dots & U_{NM} \end{vmatrix} \cdot \begin{vmatrix} s_1 & 0 & 0 \\ \dots & \dots & \dots \\ 0 & 0 & s_N \end{vmatrix} \cdot \begin{vmatrix} V_{11}^T & \dots & V_{N1}^T \\ \dots & \dots & \dots \\ V_{N1}^T & \dots & V_{NN}^T \end{vmatrix}, \quad (A1)$$

with  $U$  and  $V$  being orthogonal, i.e.,

$$\sum_i U_{ia} U_{ib} = \delta_{ab}, \quad \sum_i V_{ia} V_{ib} = \delta_{ab}, \quad (A2)$$

or

$$U^T \cdot U = \mathbf{1} \ , \quad V^T \cdot V = \mathbf{1} \quad (A3)$$

and  $s$  being diagonal.

In this work we are interested just in the case when  $M = N$  and all matrices are square; accordingly, it is also  $U \cdot U^T = \mathbf{1}$  (and  $V \cdot V^T = \mathbf{1}$ ).

The decomposition (A1) is unique, apart trivial multiplicative factors.

The *condition number* of the matrix  $\mathcal{M}$  is then defined as the ratio  $K$  between the largest and smallest (in magnitude)  $s_i$ . A matrix is said to be *ill-conditioned* if  $K$  is too large (or *singular* if  $K \rightarrow \infty$ ).

## 2. Norms and error magnification

Let us remind first that the (2-)norm of a vector  $\mathbf{x}$  reads

$$|\mathbf{x}| = \left[ \sum_i |x_i|^2 \right]^{1/2}$$

$x_i$  being its components. The (2-)norm of a matrix  $\mathbf{A}$  is then defined as follows:

$$|\mathbf{A}| = \max \left( \frac{|\mathbf{A} \cdot \mathbf{x}|}{|\mathbf{x}|} \right) \quad (A4)$$

i.e.:  $|\mathbf{A}|$  is the maximum factor by which the matrix  $\mathbf{A}$  can amplify a non-vanishing vector  $\mathbf{x}$ . It can then be shown that, if we perform a SVD of  $\mathbf{A}$  and  $s_1$  is the top component of the diagonal matrix  $\mathbf{s}$ , in the relation  $\mathbf{A} = \mathbf{U} \cdot \mathbf{s} \cdot \mathbf{V}^{-1}$ , it is

$$|\mathbf{A}| = s_1 \ .$$

Let us then outline that

$$\mathbf{A}^{-1} = \mathbf{V} \cdot \mathbf{t} \cdot \mathbf{U}^{-1} \ ,$$

with  $t_i = s_i^{-1}$ . Accordingly,  $|\mathbf{A}^{-1}| = 1/s_n$ ,  $s_n$  being the smallest component of the matrix  $\mathbf{s}$  and

$$|\mathbf{A}| \cdot |\mathbf{A}^{-1}| = s_1/s_n \ . \quad (A5)$$

The matrix-vector and matrix-matrix products have then the following properties:

$$|\mathbf{A} \cdot \mathbf{x}| \leq |\mathbf{A}| \cdot |\mathbf{x}| \quad (A6)$$

$$|\mathbf{A} \cdot \mathbf{B}| \leq |\mathbf{A}| \cdot |\mathbf{B}| \ .$$

Let us then assume that

$$\mathbf{A} \cdot \mathbf{x} = \mathbf{b} \quad (A7)$$

and consider  $\tilde{\mathbf{x}} = \mathbf{x} + \delta\mathbf{x}$ , as we do when we try to reobtain  $P(k, z)$  from noisy  $C_{ij}(\ell)$ . It shall be  $\mathbf{A} \cdot \tilde{\mathbf{x}} = \mathbf{b} + \delta\mathbf{b}$  and therefore

$$\tilde{\mathbf{x}} - \mathbf{x} = \mathbf{A}^{-1} \cdot \delta\mathbf{b} \ ,$$

so that, owing to eq. (A6),

$$|\delta \mathbf{x}| \leq |\mathbf{A}^{-1}| \cdot |\delta \mathbf{b}|.$$

In turn, eq. (A7) yields

$$\frac{1}{|\mathbf{x}|} \leq \frac{|\mathbf{A}|}{|\mathbf{b}|}$$

and, therefore

$$\frac{|\delta \mathbf{x}|}{|\mathbf{x}|} \leq |\mathbf{A}| \cdot |\mathbf{A}^{-1}| \cdot \frac{|\delta \mathbf{b}|}{|\mathbf{b}|}.$$

Owing to eq. (A5) we have then that

$$\frac{|\delta \mathbf{x}|}{|\mathbf{x}|} \leq \frac{s_1}{s_n} \cdot \frac{|\delta \mathbf{b}|}{|\mathbf{b}|}. \quad (\text{A7})$$

i.e., that error magnification is surely smaller than the ratio between the maximum and minimum  $s$  components considered, coinciding with the *condition number*  $K$ .

For more details on this Section and proofs of the theorems, besides of [18, 19], see also [20].

### 3. Gauss–Laguerre parameter selection

The Gauss–Laguerre sum, replacing the integration over  $P(k, z)$  to obtain the shear spectra  $C_{ij}(\ell)$ , ought to be made with an eye to the matrix inversion which will follow. The condition number  $K$  of the matrix  $\mathcal{M}$ , in fact, depends in a critical way on the selection of the  $\bar{u}$  and  $\beta$  parameters used in the change of variable  $x = (u/\bar{u})^\beta$ . A bad selection of  $\bar{u}$  and  $\beta$  can yield  $K$  values up to  $10^{20}$  or even larger. Moreover,  $K$  is also directly linked to error magnification, according to eq. (A7).

To minimize  $K$  we can act on three parameters: besides of  $\beta$  and  $\bar{u}$ , we must take into account  $N_{cut}$ , the number of  $s_i$  which (unavoidably) will be set to zero. Increasing  $N_{cut}$  obviously reduces  $K$ , but our aim amounts to minimize  $K$  while keeping  $N_{cut}$  sufficiently low, so to grant a fair and physical solutions to the a substantial part of the 28 equations forming the linear system.

Let us then keep into account that the galaxy redshift distribution  $n(z)$  rapidly declines beyond  $z \sim 1$  and that, therefore, the window functions  $W_r$  and the  $\mathcal{M}$  matrix element also fade. In the following we shall not directly consider contributions coming from above a maximum redshift  $z_{max} = 1.4$ , corresponding to a maximum comoving distance  $u_{max} = 4194 \text{ Mpc}$ , a choice yielding fair results. We shall then select the value of  $\bar{u}$  so that

$$\bar{u}(\beta) = \frac{u_{max}}{x_M^{1/\beta}}$$

$x_M$  being the largest node in the Gauss-Laguerre integration.

With this rule, we can then estimate the condition number for a wide range of  $\beta$  (from 0.1 to 3.5) and  $N_{cut}$  values. The latter parameter will be considered in the interval 0 (we keep all singular values) – 26 (keeping only the two largest singular values to estimate their ratio).

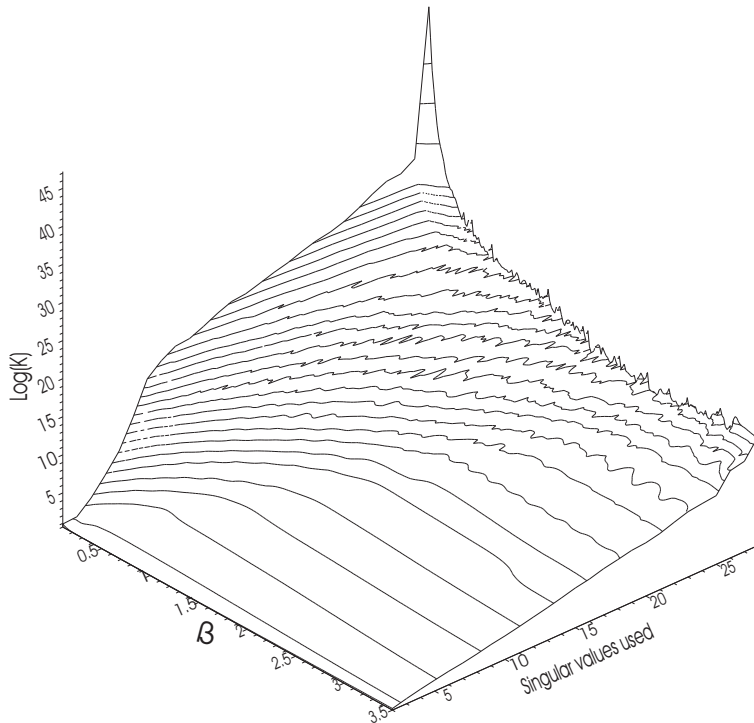


**Figure 15:** The condition number  $K$  is plotted against  $\beta$  and the number of non-zero  $s_i$  kept. At high  $K$ , there appear some graphic irregularities in the curves, due to the discreteness of the  $s_i$  number.

In Figure 15,  $K$  is plotted as a function of  $\beta$  and of the residual  $s_i$  number ( $28 - N_{cut}$ ). The plot shows how dramatically  $K$  blows up just by choosing unsuitable values of the free parameters. It is also evident that, reducing the number of non-zero  $s_i$ ,  $K$  systematically decreases and that, for a given number of non-zero  $s_i$ ,  $K$  depends on  $\beta$ .

However, when the number of non-zero  $s_i$  is small ( $< \sim 10$ ) the  $K$  dependence on  $\beta$  weakens. This can be exploited to perform slight changes of the  $\beta$  value, yielding a suitably different set of  $u_r$  for the Gauss-Laguerre nodes  $x_r$ . In this way, we can obtain  $P(k)$  at almost any  $z$  value, in the  $z$ -range where matrix inversion is efficient (see text).